Low-energy avionic piezoelectric deicing system

Modar Jomaa, Pierre-Etienne Lévy, Dejan Vasic, François Costa, Marwan Ali

Low-Energy Avionic Piezoelectric Deicing System

Modar JOMAA[1,4], Pierre-Etienne LÉVY[1], Dejan VASIC[2], François COSTA[3] and Marwan ALI[4]
[1]Université Paris-Saclay, ENS Paris-Saclay, CNRS, SATIE, 91190 Gif-sur-Yvette, France
[2]Université de Cergy-Pontoise, 95031 Cergy-Pontoise, France
[3]Université Paris Est Créteil, INSPE, 94000 Créteil, France
[4]Safran Tech, groupe de recherche E&E, 78117 Magny-Les-Hameaux, France
E-mail: modar.jomaa@ens-paris-saclay.fr

***Abstract*—Piezoelectric actuators are widely used in several applications and are becoming increasingly attractive in aircraft and industrial contexts, mainly when efficiency and economical energy conversion are required. One of these applications is the Avionic Piezoelectric Deicing System. Piezoelectric actuators are considered as a potential solution for developing a low-energy ice protection system for aircraft. This type of system applies vibration to the structure by activating its own resonant frequencies to generate sufficient stress to break the ice and cause it to delaminate from the substrate. The deicing mechanism depends strongly on the chosen excitation mode, whether it's flexural (bending) mode, extension (stretching) mode, or a combination in between, hence affecting the efficiency and effectiveness of the deicing process.**

In this contribution, a proof of concept of a deicing system utilizing lightweight piezoelectric actuators with minimal power requirement is proposed. Deicing was demonstrated with a power input density of 0.074 W/cm² and a surface ratio of 0.07 piezoelectric actuators per cm². First, a numerical method for positioning piezoelectric actuators and choosing the proper resonance mode was validated to assist in the system's design. Then, the numerical method was used to implement piezoelectric deicing on a more representative structure of an aircraft wing or nacelle. Finally, a converter topology adapted for deicing application was proposed.

***Keywords*—Deicing, piezoelectric actuator, extensional mode, fracture mechanism, resonant inverter, PWM inverter, soft-**

NOMENCLATURE

u	displacement, m
σ	stress tensor, Pa
λ	wavelength, m
c	wave propagation speed in the medium, m/s
n	resonant mode number
f	resonance frequency, Hz
ω	resonance angular frequency, rad/s
k	angular wave number
ε	strain tensor, m/m
E	Young's modulus, MPa
υ	Poisson's ration
ρ	volumetric mass density, kg/m^3
L	plate length, m
PWM	Pulse Width Modulation
EMC	Electromagnetic Compatibility
ZVS	Zero Voltage Switching
ZCS	Zero Current Switching
GaN	Gallium Nitride
MEA	More Electric Aircraft

I. INTRODUCTION

Environmental constraints and their impact on public opinion have led the aircraft industry to accelerate the energy transition in aeronautics toward a "More Electric Aircraft" (MEA). We are, therefore, witnessing a gradual increase in the role of electrical energy in onboard applications [1]. This electrification trend aims to replace all non-propulsive systems (hydraulic and pneumatic) with electromechanical alternatives in order to optimize aircraft performance, decrease operating and maintenance costs, increase dispatch reliability, and reduce gas emissions [2]. Among the systems underscored by this transition is the deicing system.

Since ice accretion on aircraft wings and nacelles can significantly impact aerodynamic efficiency and balance, resulting in reduced lift and increased drag, aircraft require an ice protection system capable of meeting the demands of various certifications for full-icing clearance. A variety of deicing methods that defer by the energy used are employed today to prevent ice formation. These include: turbine engine bleed air, pneumatic deicing boot system, chemical fluid, and electrically heated systems [3]. However, these methods are classified as very energy-consuming and are only suitable for some aircraft categories. Concerning electromechanical technologies such as electro-impulsive [4], electro-expulsive [5], and piezoelectric [6], the latter stands out as the most promising solution in terms of power consumption, weight, and cost-effectiveness.

In the literature, different approaches using piezoelectric actuators have been explored. First, it was investigated by Ramanathan et al [7], where experiments on resonant deicing systems were performed at very high frequencies to generate ultrasonic surface waves to produce shear stress at the ice/substrate interface. However, the deicing occurred through a thermal action. Experiments of deicing on low frequencies were carried out in the studies of Venna et al. [8], and Struggl et al. [9]. Yet, limited deicing performance. Kandagal and Venkatraman [10] partially deiced a simple flat plate with piezoelectric actuators by exciting resonant frequencies.

Villeneuve et al. [11] worked on deicing a rotorcraft blade by studying actuator positioning and activation strategies. Partial deicing was achieved. Budinger et al. [12] compared different architectures of deicing based on piezoelectric actuators and on the use of structural resonance modes. However, only tests with Langevin piezoelectric transducers were performed and where some delamination has occurred. In Budinger et al. [13], fracture mechanisms were analyzed. Key performance indicators were proposed to analyze the performance of such systems regarding fracture propagation. This paper aims to produce a numerical model of a piezoelectric system in order to investigate crucial design parameters such as actuator positioning and sequencing, and then validate it through an experimental setup. A converter topology adapted to piezoelectric actuators for deicing applications was selected and developed to drive the deicing system.

II. Piezoelectric Deicing System

The operating principle of the piezoelectric deicing system is to create microscopic ultrasound mechanical vibrations based on the converse effect (reverse piezoelectric effect). Depending on the resonance mode, these electromechanical vibrations produce a stress field that initiates cohesive fractures in the ice, adhesive fracture at the interface leading edge/ice, or both [13]. Two configurations were introduced in the literature for using piezoelectric actuators. The first configuration with the Langevin transducer was used for its ease of installation using bolts, and the lower risk of mechanical failure due to their prestressed structure which allows them to withstand higher stresses during operation. However, the utilization of prestressed PZT ceramics, mainly designed to stimulate structural flexural modes, can, in the best cases result in some ice delamination [14]. This issue, coupled with their substantial weight, make them less advantageous. The second configuration with piezoelectric patches which can be glued to the mechanical structure was the most commonly tested in the literature and seemed to be more promising (Fig. 1).

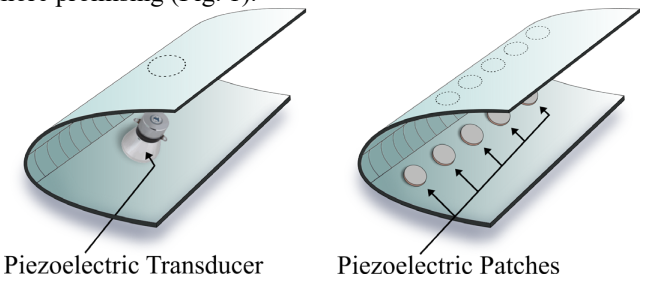

Fig. 1. Configuration of a piezoelectric de-icing system with piezoelectric patches and transducers.

A. Ice characterization

Numerous studies and experiments have been carried out to determine the adhesive and cohesive strength of ice on various materials and under diverse icing conditions [9] [15],[16],[17],[18],[19],[20]. These studies revealed that the expected adhesive shear strength value of refrigerated glaze ice can be estimated to be between 0.24 MPa and 1.7 MPa. The average adhesion shear strength of freezer ice to steel at -10°C was experimentally measured to be 1.5 MPa and the maximum was found to be at 1.66 MPa [21] while the cohesive tensile strength was found to be between [0.6 – 3] MPa [22],[23] [24]. Glaze ice characteristics are listed in table TABLE I.

TABLE I
Glaze Ice Characterization

Glaze ice	
Young's modulus (E)	9.3 GPa
Poisson's ratio (υ)	0.325
Density (ρ)	900 kg/m^3
Cohesive strength	[0.6 - 3] MPa
Adhesive strength	[0.24 – 1.7] MPa

B. Deicing mechanisms

The propagation of fractures after their initiation depending on the deicing mechanism has been stated in [25]. The first mechanism starts when tensile stress exceeds ice tensile strength leading to a cohesive fracture at the top of the ice layer which then propagates through the ice until the bottom at the ice/substrate interface. Consequently, adhesive fractures occur at this point, leading to ice delamination (Fig. 2). Cohesive fractures alone are insufficient for deicing as ice can stick to the surface on which it is accreted. Therefore, they should always be coupled with adhesive fractures to allow ice debonding. The second mechanism starts when shear stress exceeds the ice/substrate interface shear strength leading to the initiation of an adhesive fracture and then the propagation of this adhesive fracture.

The examination of these two mechanisms has been conducted in the context of flexural and extensional modes. It has been shown that the first mechanism is triggered by flexural modes [25],[26], whereas the second mechanism has been reported for extensional modes at high frequencies (32 kHz) [27], [28]. This contribution concentrates on the second mechanism of deicing using extensional modes.

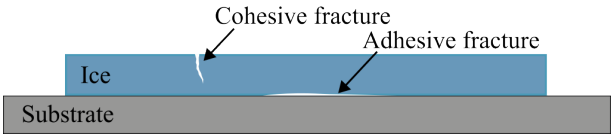

Fig. 2. Cohesive and adhesive fracture illustration.

C. *Analytical and finite element analyses*

In order to demonstrate the concept of piezoelectric deicing through the second fracture mechanism, validation of a numerical model of a piezoelectric deicing system applied to a simple flat plate structure had to be done. An aluminum alloy A5 1050 plate (150 mm × 50 mm × 1.5 mm) with one round hard PZT (PIC181) piezoelectric ceramic (ø 20 mm, 1 mm) bonded underneath in the center using epoxy resin, was modeled numerically in 3D using the finite element software COMSOL (Fig. 3). Its impedance was computed and compared to the measured one (Fig. 4). The sample is held in free boundary conditions. The round shape of piezoelectric ceramic was chosen since it suffers less stress on the edges than a rectangular shape (any shape with angles) [29].

Since we are interested in the second fracture mechanism, the latter is only being studied and tested. Due to the geometry of the chosen plate, the dominant extensional mode will be along the x axis and will be at lower frequencies than the extensional mode along the y axis. To simplify the problem, displacements along the y and z axis will be neglected. This leads us to solve a one-dimensional problem.

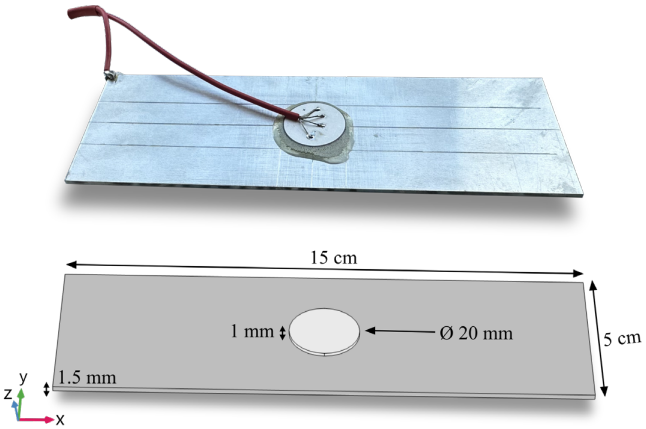

Fig. 3. 3D finite element modeling and reel image of the plate.

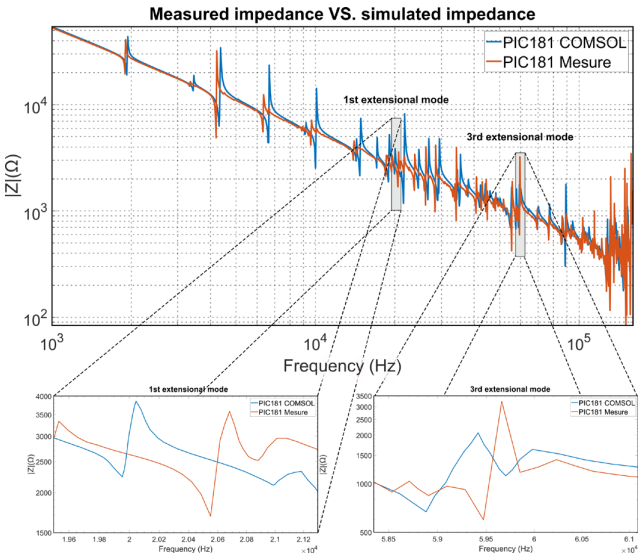

Fig. 4. Measured impedance vs. simulated impedance of the structure (plate + piezoelectric ceramic)

Wave equation:

$$\Delta\vec{E} = \frac{1}{c^2}\frac{\partial^2\vec{u}}{\partial t^2} \tag{1}$$

$$\frac{\partial^2\vec{u}}{\partial x^2} + \frac{\partial^2\vec{u}}{\partial y^2} + \frac{\partial^2\vec{u}}{\partial z^2} = \frac{1}{c^2}\frac{\partial^2\vec{u}}{\partial t^2} \tag{2}$$

Where $\vec{E}$ is the mechanical wave vector, $\vec{u}$ is the displacement vector, and C is the wave propagation speed in the medium. We are only looking for extension modes along the length of the plate:

$$\frac{\partial^2\vec{u}}{\partial x^2} = \frac{1}{c^2}\frac{\partial^{2\vec{u}}}{\partial t^2} \tag{3}$$

For a standing wave:

$$u(x,t) = f(x).g(t) \text{ with } \begin{cases} f(x) = \cos(kx + \Psi) \\ g(t) = \sin(\omega t + \varphi) \end{cases} \tag{4}$$

Derived Hooke's law for shear stress of a uniform bar:

$$\sigma = E.\varepsilon = E\frac{\partial u}{\partial x} \tag{5}$$

Since the plate has free boundary conditions:

$$\sigma(0,t) = 0\,, \sigma(L,t) = 0 \tag{6}$$

From (5) and (6):

$$\sin(\Psi) = \sin(kL + \Psi) = 0 \tag{7}$$

With $k = \frac{w}{c} = \frac{2\pi}{\lambda}$ is the angular wave number.

Then, from (7):

$$\Psi = 0 \quad \text{and} \quad \mathrm{kL} = \mathrm{n}\pi \tag{8}$$

Condition for the existence of a standing wave:

$$\lambda = \frac{2L}{n} \quad \text{with} \quad n \in \mathbb{R}^* \rightarrow f_n = \frac{n.c}{2L} \tag{9}$$

General stationary solution:

$$u(x,t) = \sum_{n=1}^{+\infty} A_n.\cos\left(\frac{n\pi}{L}x\right).\sin\left(\frac{n\pi}{L}c.t + \varphi_n\right) \tag{10}$$

$$\sigma(x,t) = \sum_{n=1}^{+\infty} B_n.\sin\left(\frac{n\pi}{L}x\right).\sin\left(\frac{n\pi}{L}c.t + \varphi_n\right) \tag{11}$$

Case 1: only one actuator placed in the middle of the plate.

$$\begin{cases} \sigma(x_p,t) = \sigma_p.g(t) \\ \forall n, \quad \varphi_n = 0 \end{cases} \tag{12}$$

$$g(t) = \sin\left(N\pi\frac{c.t}{L}\right)$$

From (11) and (12):

$$\sigma_p.\sin\left(N\pi\frac{c.t}{L}\right) = \sum_{n=1}^{+\infty} B_n.\sin\left(\frac{n\pi}{L}x_p\right).\sin\left(\frac{n\pi}{L}c.t\right)$$

Then:

$$\begin{cases} n = N, & \sigma_p = B_n . \sin\left(\frac{N\pi}{L} x_p\right) \\ \forall n \neq N, & 0 = B_n . \sin\left(\frac{N\pi}{L} x_p\right) \end{cases}$$

Finally:

$$\sigma_p = \begin{cases} -1^{\frac{N-1}{2}} . B_n & if\ N\ odd \\ 0 & if\ N\ even \end{cases} \quad (13)$$

For this study case, only the fundamental extensional mode and its odd harmonics will appear in the plate as demonstrated in equation (13).

In simulations, in order to filter all other resonance modes except extensional modes, zero displacements are imposed along the y and z axis. According to computations, the first extensional mode (fundamental) is found around 20 kHz which verifies the equation (9) where c = 6300 m/s for aluminum (Fig. 4 and Fig. 5). However, when the displacement is set to be free on the three axes, the extensional mode will be coupled with flexural modes and other parasitic modes, making it difficult to be observable around 20 kHz (Fig. 6). On the other hand, when driving the piezoelectric actuator at the 3rd extensional mode which is spotted around 60 kHz (Fig. 4 and Fig. 7), the extensional mode is still dominant even when displacement is set to be free on the three axis (Fig. 8). Also, the stress level obtained (mainly shear stress) is much higher than the 1st extensional mode. In order

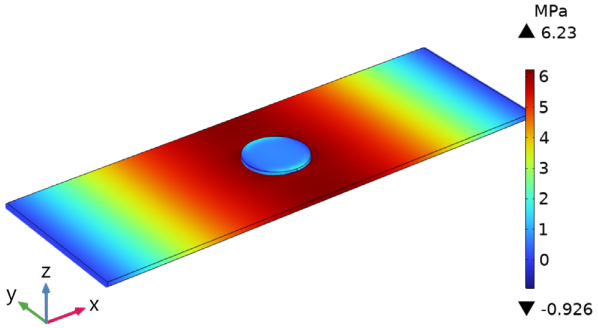

Fig. 5. Shear stress levels at the 1st extension mode at 20 kHz with zero displacements imposed on the y and z axis.

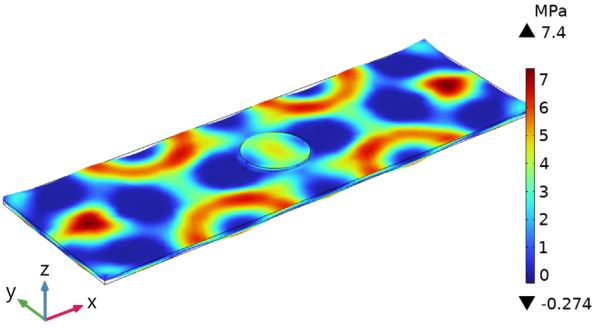

Fig. 6. Stress levels at the 1st extension mode around 20 kHz with free displacement on the x, y and z axis.

to amplify the 3rd extensional mode, two other ceramics were bonded to the plate at the extensional wave crests/troughs as in Fig. 9.

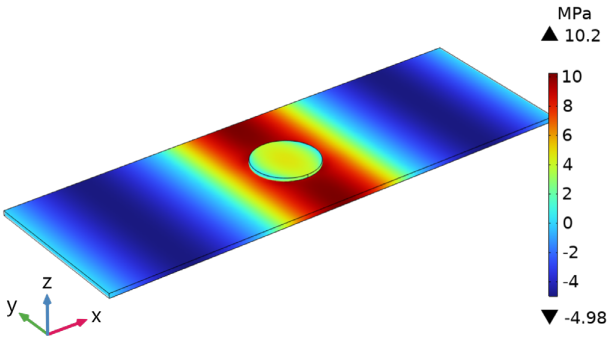

Fig. 7. Shear stress levels at the 3rd extension mode at 59 kHz with zero displacements imposed on the y and z axis.

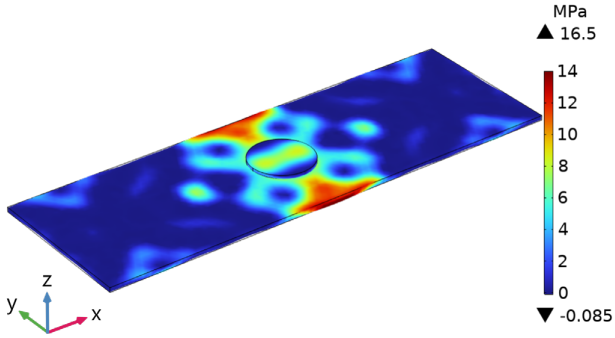

Fig. 8. Shear stress levels at the 3rd extension mode at 59 kHz with free displacement on the x, y and z axis.

Case 2: For three actuators placed at:

$$x_1 = \frac{L}{6}, x_2 = \frac{L}{2}, \text{and } x_3 = \frac{5L}{6} :$$

From (11) and (12):

$$\begin{cases} \sigma(x_1, t) = \sigma_1 . g(t) \rightarrow \sigma_1 = B_1 . \sin\left(n\frac{\pi}{6}\right) \\ \sigma(x_2, t) = \sigma_2 . g(t) \rightarrow \sigma_2 = B_2 . \sin\left(n\frac{\pi}{2}\right) \\ \sigma(x_3, t) = \sigma_3 . g(t) \rightarrow \sigma_3 = B_3 . \sin\left(n\frac{5\pi}{6}\right) \end{cases}$$

Were $B_1 = B_2 = B_3 = B$, since the three actuators are the same.

Then:

TABLE II
STRESS DISTRIBUTION BASED ON ACTUATOR POSITIONING AND THEIR POLARIZATION

n	σ_1	σ_2	σ_3	Polarization
1	$B/2$	B	$B/2$	↑ ↑ ↑
2	$B.\sqrt{3}/2$	0	$-B.\sqrt{3}/2$	↑ × ↑
3	B	$-B$	B	↑ ↓ ↑
4	$B.\sqrt{3}/2$	0	$-B.\sqrt{3}/2$	↑ × ↓
5	$B/2$	B	$B/2$	↑ ↑ ↑
6	0	0	0	× × ×

Polarization refers to the electric polarization direction of the actuators. The applied voltage on the three actuators will be like indicated in the 3rd case (mode 3) of TABLE II, and as illustrated in Fig. 9. Computation results show as expected, a zero shear stress level for the first mode (Fig. 10) since the actuators C1 and C3 are put in opposition to the actuator C1. In contrast, at the 3rd mode, the shear stress level obtained is approximately three times higher compared to when only one

actuator is used (Fig. 11, Fig. 12 and Fig. 13).

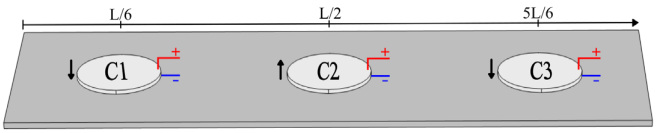

Fig. 9. Position, polarization and feeding direction of the three ceramics.

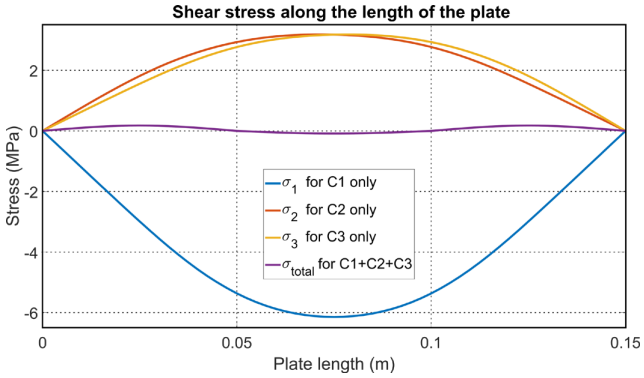

Fig. 10. Shear stress level traced along a line that runs the length of the plate at the 1st extension mode for one actuator at a time, and then all three together.

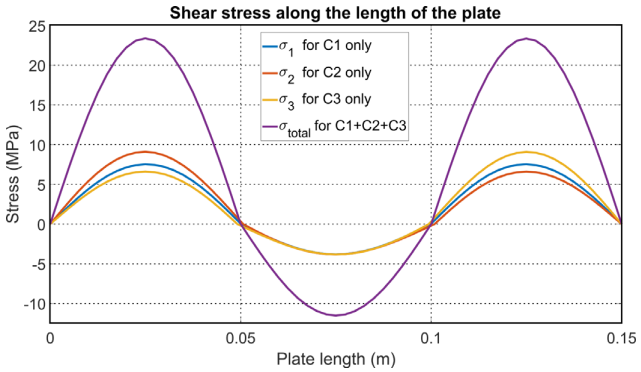

Fig. 11. Shear stress level traced along a line that runs the length of the plate at the 3rd extension mode for one actuator at a time, and then all three together.

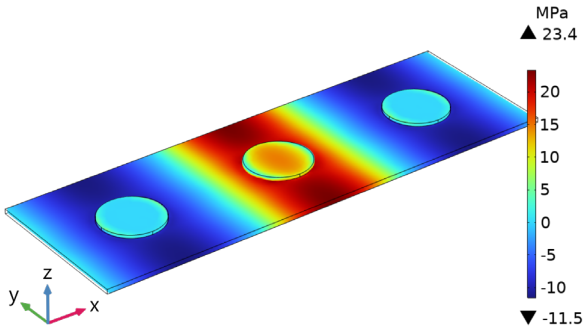

Fig. 12. Shear stress level at the 3rd extension mode at 59 kHz with zero displacement imposed on the y and z axis.

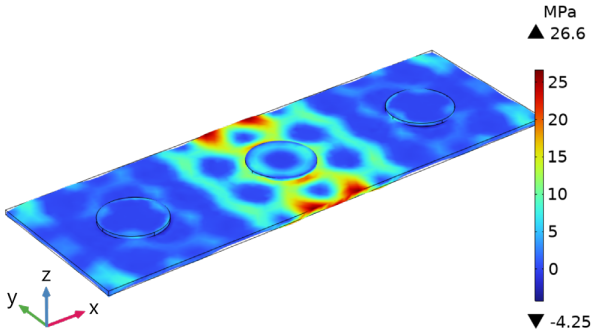

Fig. 13. Shear stress level at the 3rd extension mode around 59 kHz with free displacement on the x, y and z axis.

A. Experimental Validation

After validating the analytical approach for positioning piezoelectric actuators to stimulate extensional modes through simulations, experimental validation becomes essential to illustrate the effectiveness of this methodology.

The setup consists of an aluminum alloy A5 1050 plate (150 mm × 50 mm × 1.5 mm) with rounded hard PZT (PIC181) piezoelectric ceramics (ø 20 mm, 1 mm) bonded underneath using epoxy resin. A glaze ice layer of approximately 2 mm thickness was accreted to the surface of the aluminum plate at a temperature of -18 °C. A Class-AB linear amplifier with a function generator were used to deliver the appropriate voltage level and frequency to the actuators.

Case 1: only one actuator placed in the middle of the plate. The actuator was driven at around 20 kHz, corresponding to the first extensional, using a sinusoidal voltage with a magnitude of 200 V. At the first extensional mode where it is coupled with other modes like showed in simulation results (Fig. 6), the stress level (combining shear and tensile) was not sufficient for cracking or debonding the 2 mm glaze ice layer. Experimentally, as shown in Fig. 14, no significant events occurred. On the other hand, for the 3rd extensional mode at approximately 60 kHz (Fig. 7 and Fig. 8), the stress level, mainly shear stress, was higher, leading to some cohesive fractures but mainly adhesive fractures as illustrated in Fig. 15. The process starts with two cohesive fractures (bulk

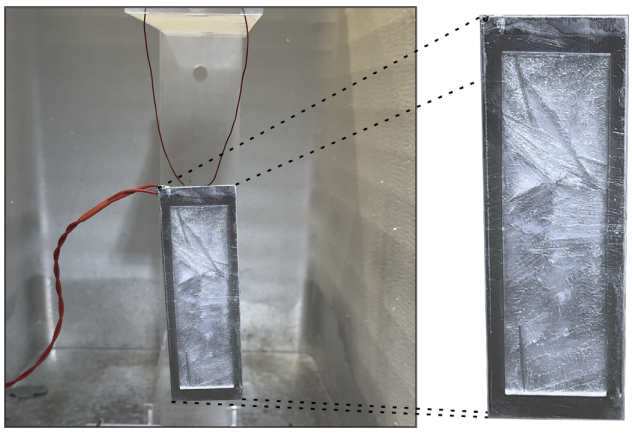

Fig. 14. Experimental setup of the aluminum plate with 2 mm glaze ice thickness.

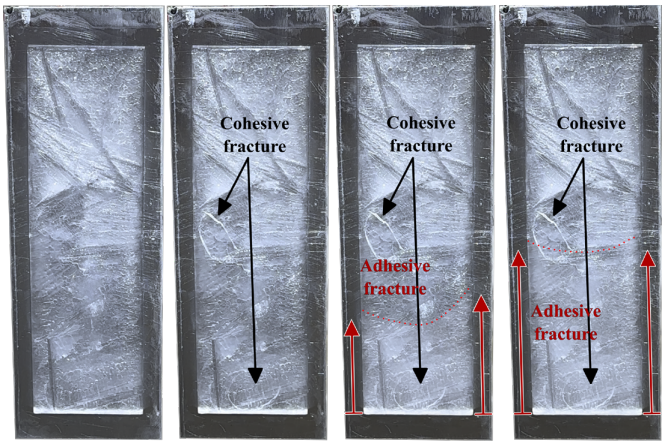

Fig. 15. Cohesive fractures and propagation of adhesive fracture at the 3rd extension mode.

fractures) due most likely to parasitic modes, followed by adhesive fracture at the bottom of the ice layer, then the propagation of this adhesive fracture as illustrated by the red arrows in Fig. 15. However, the shear stress magnitude was insufficient for a complete debonding of the ice layer.

Case 2: For three actuators placed at:

$$x_1 = \frac{L}{6}, x_2 = \frac{L}{2}, \text{and } x_3 = \frac{5L}{6}$$

Since ice accretion is not uniform and homogenous in a real-life application (ice accretion on aircrafts), its shear and cohesive strength could vary from the values given previously in the literature (TABLE I). Therefore, stress levels generated by the actuator should be great enough to ensure a complete deicing regardless ice formation conditions. To do so, two other actuators were bonded to the plate at the extensional wave crests/troughs, and in opposition of polarization to the one in the middle as in Fig. 9, in order to amplify the 3rd extensional mode. As a result, we get in experimentation tests for the 3rd mode multiple cohesive fractures at the beginning, followed by adhesive fractures and then a complete debonding of the ice.

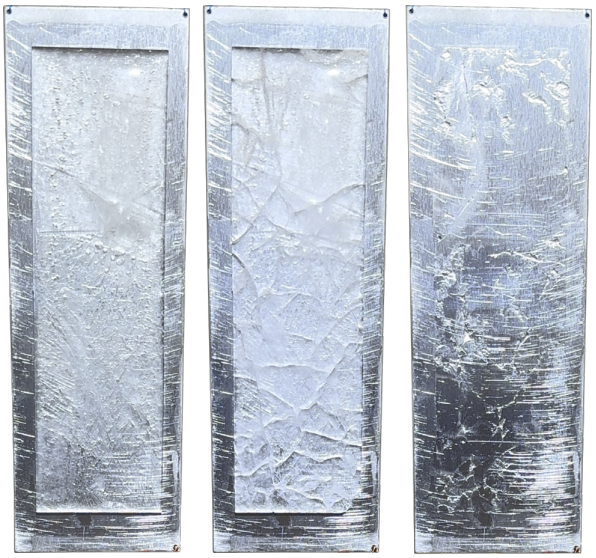

Fig. 16. Experimental result of deicing a 2 mm glaze ice layer at the 3rd extension mode of the rectangular plate.

These three steps occur instantaneously at 200 V, taking place within a span of approximately 5 seconds as shown in Fig. 16. The multiple cohesive fractures were most likely due to the fact that the global shear stress level on the whole plate mutually entailed cohesive stress which exceeded the cohesive strength which subsequently led to its fracture, without neglecting the impact of the other parasitic modes.

Case 3: Representative Piezoelectric Deicing Model

Following the validation of the numerical model of the small plate with the experimental setup, a more representative model was made. A large plate of aluminum of 350 mm × 250 mm × 1.5 mm dimension with 20 actuators with the same dimensions and material as used previously were employed to create the finale setup. The same strategy was used for driving and placing the actuators, and also the same icing conditions to

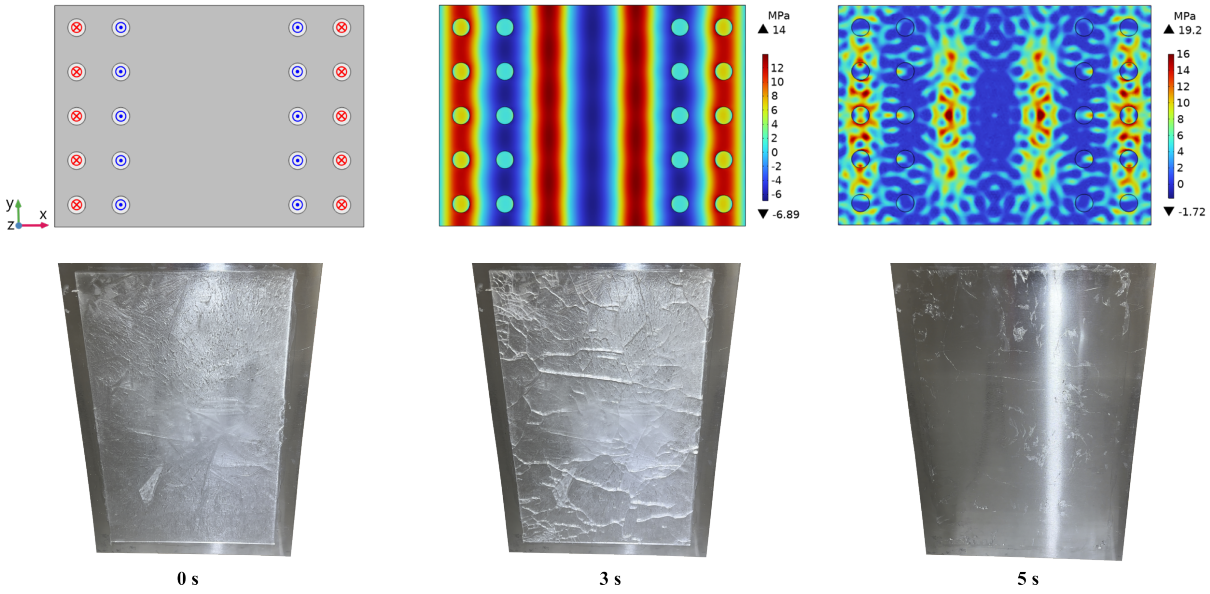

Fig. 17. Computation result of the 7th extension mode and its corresponding experimentation results.

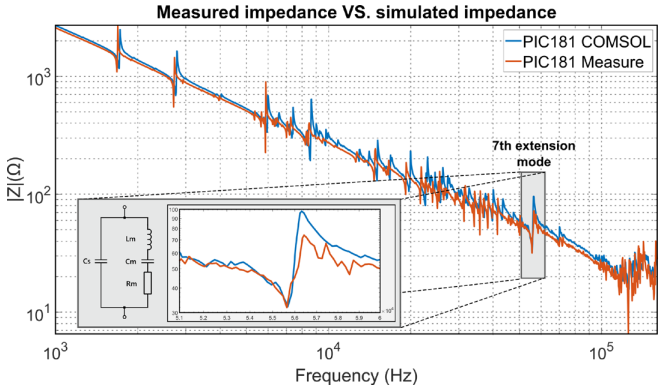

Fig. 18. Van Dyke circuit model of the setup in Fig. 17 around the 7th extension mode.

form a 2 mm glaze ice layer were ensured. As illustrated in Fig. 17, actuators were placed in a way to amplify the 7th extension mode at 55 kHz where we get enough stress level and thus enough displacement to crack and delaminate the ice. Similarly to case 2, in experimental tests, we observe multiple cohesive fractures initially, followed by adhesive fractures, and then complete debonding of the ice. These three stages occur at 200 V, taking place within approximately 5 seconds, as illustrated in figure 16 (⊗ and ⊙ refer to the actuator polarization direction).

III. ELECTRICAL SPECIFICATIONS OF THE SYSTEM

In order to properly drive a piezoelectric actuator and improve its performance, it is essential to know its electrical characteristics. The most common equivalent circuit that characterizes a piezoelectric actuator around its resonance frequency is the Van Dyke model. In this model, we identify the static capacitance Cs paralleled with a motional branch (Lm, Cm, Rm). Each piezoelectric actuator has several resonance frequencies in which its impedance has a lower magnitude as compared to non-resonance frequencies. To attain higher efficiency and deliver more power to the ultrasound system, actuators should be excited at their dominant resonance frequency which corresponds in our case to the 7th extension mode at 55 kHz (Fig. 18).The deicing system and its power supply must comply with the aviation regulations and standards (DO 160), as well as the installation constraints of the equipment (safety, space requirements), while allowing its proper operation. The power supply should deliver a sinusoidal voltage to the actuators in order to excite the desired mode. Otherwise, undesired harmonics (low-quality signal) can deteriorate the actuator's performance and increase power consumption in the system. Finally, given the space constraints that do not allow to place the converter to be as close as possible to the load (actuators), the latter will be fed through 2 meters long cables (Fig. 19).

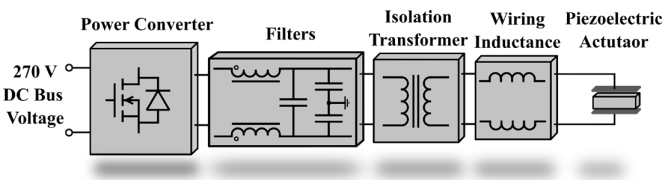

Fig. 19. Synoptic board of the complete system.

IV. DISCUSSION ON THE DRIVING POWER SUPPLY FOR OPTIMIZED FEEDING OF THE PZT ACTUATORS

Since the electrical behavior depends on the mechanical load and the temperature [29], it is essential to consider some aspects when designing the power supply. One is the driving frequency which must correspond to the mechanical resonance frequency of the actuators attached to the leading edge. In fact, at this resonance, the power transfer is better, and the reactive energy consumption is reduced (less losses). Another important aspect is the quality of the excitation signal, which has an important role in the piezoelectric actuator's performance and lifetime [30]. In this context, several techniques are proposed in the literature [31],[32],[33]. Linear power amplifiers (A, B, AB, ...) are used to feed piezoelectric loads because they can generate signals with low harmonic distortion rates. However, they have low efficiency and are often bulky and heavy. Therefore, switched-mode power supplies are more and more used and dominate the market because of their good efficiency and high-power density.

In this regard, various literature has focused on driving piezoelectric actuators using voltage source inverters. Resonant inverters (LC or LLCC) and PWM inverters (LC or LLCC) are the most commonly used. Other topologies have been used, such as the three-level NPC inverter and the current inverter [7]. The main disadvantages of resonant inverters are the volume and weight of the magnetic elements of the resonant filter and a very limited variation of the operating frequency. To overcome these drawbacks, PWM-controlled inverters (LC or LLCC) have been proposed [34]. The disadvantages of PWM control are often related to the switching frequency, which generates high switching losses and EMC (Electromagnetic Compatibility) problems. These issues can be particularly limiting in some cases, especially when GaN transistors are employed.

In [35], an investigation of three interesting topologies for driving ultrasound piezoelectric actuators under aeronautical constraints was conducted. The study revealed the predominance of the ARCPI (Auxiliary Resonant Commutated Pole Inverter) structure over the current source inverter (CSI) and the Energy Recovery "Resonant" structure.

A. Auxiliary Resonant Commutated Pole Inverter (ARCPI)

Several soft-switching inverter topologies have been proposed in the literature [36], [37], [38]. This type of inverter aims to achieve high-frequency operation with reduced switching losses and electromagnetic interference (EMI). An interesting example of soft-switching inverters of the "Resonant Pole Inverter (RPI)" family is the Auxiliary Resonant Commutated Pole Inverter (ARCPI) [39], [40],[41]. The circuit topology is illustrated in Fig. **20**.

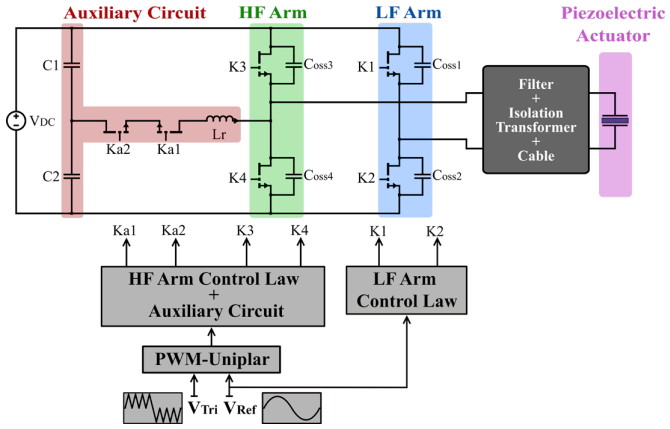

Fig. 20. Circuit topology of the ARCP Inverter.

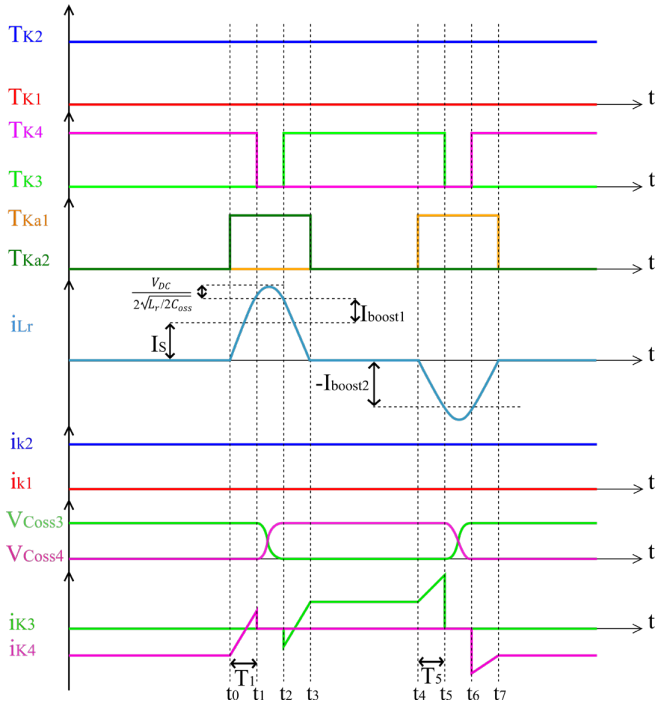

Fig. 21. ARCPI theoretical waveforms.

The inverter consists of two main arms and an auxiliary circuit connected to a capacitive divider bridge. In order to limit losses as well as the number of components, one arm is switched at Low Frequency (LF) synchronized to the transducer frequency, and the other is switched at High Frequency (HF), on which the auxiliary circuit is connected. The role of this circuit is to charge and discharge the parasitic capacitances C_{oss} to ensure ZVS condition on the HF arm. On the other hand, the control law of the auxiliary circuit implies zero current switching (ZCS) of its transistors. Moreover, since the auxiliary circuit is not in the main power path, the power rating of its switches will be reduced compared to that of the main switches. The control applied is a unipolar PWM which reduces the output voltage harmonics.

B. Experimental validation of the whole system

The experimental setup of the ARCP Inverter was built in the laboratory, as shown in Fig. 22, in order to drive the piezoelectric deicing system while respecting aeronautical

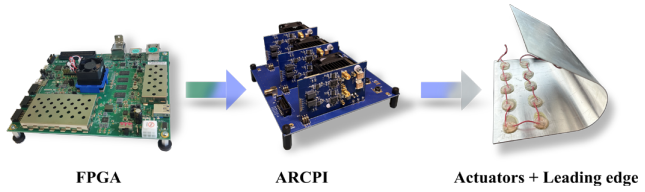

Fig. 22. Experimental setup of the complete deicing system.

constraints. The control of the inverter has been implemented in an FPGA to achieve a high precision on the driving frequency. The LF arm is switched at low frequency (55 kHz) synchronized to the output voltage while the HF arm is switched at high frequency at 2 MHz, under 270 Vdc bus voltage.

A more representative model of a wing's or nacelle's leading edge was created. An aluminum plate with the same dimension as for the case 3 (Fig. 23) and the same number and distribution of actuators was used. The aluminum plate was then curved to replicate a section of a leading edge. The curve didn't have any significant impact on the extensional wave propagation along the length of the plate. Thus, with this new setup we still have the 7th extension mode at 55 kHz as previously. At this frequency, an instantaneous cracking and delamination of 2 mm-thick-ice occurred with a power input density of 0.074 W/cm² and a surface ratio of 0.07 piezoelectric actuators per cm². However, the driving power converter should be sized to deliver at least 0.41 VA/cm² to the actuators due to their capacitive behavior and the voltage level needed to initiate fractures in the ice.

Compared to other deicing and anti-icing solutions already employed in some aircraft, such as the hot air bleed system or electrothermal system, the piezoelectric deicing system is much more economical in terms of power consumption. According to studies, the specific power required to achieve ice protection using hot bleed air system would be up to 420 kW for an Airbus A320 which corresponds to 25 kW/m² [42]. The power required to protect the Boeing 787 wings using electrothermal deicing is between 45 kW and 75 kW, which corresponds to a power requirement estimated to 3.61 kW/m² [43].

TABLEAU III
POWER REQUIREMENT COMPARISON

Deicing solution	Power requirement
Hot Bleed Air System	25 kW/m²
Electrothermal System	3.61 kW/m²
Piezoelectric System	0.74 kW/m²

CONCLUSION

The concept of deicing of wing's or nacelle's leading edge using piezoelectric actuators was demonstrated. Deicing was achieved using structural extension modes to ensure a sufficient shear stress level for ice delamination and complete deicing. It was showed through finite element simulation that its difficult, and even impossible, to excite a resonance mode alone (extension or flexural) without having parasitical

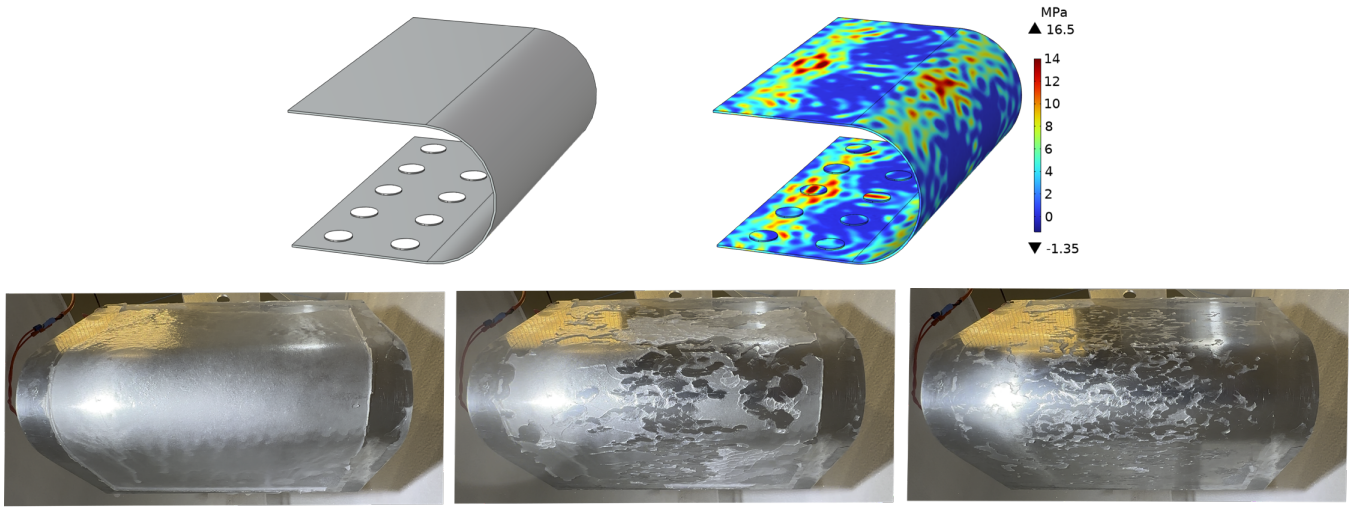

0 s **3 s** **5 s**

Fig. 23. Computation result of the 7th extension mode and its corresponding experimentation results.

modes. This was confirmed through multiple experimentation tests where deicing always involved cohesive and adhesive fractures before achieving a complete deicing.

Analytical model, supported by COMSOL finite element simulations were used to determine the proper excitation mode and the positioning of piezoelectric actuators.

A converter topology adapted to drive piezoelectric actuators was chosen and developed in the laboratory, through which, an adequate amount of power was delivered to ensure deicing. Experimental results showed complete deicing with a power input density of 0.074W/cm² and a ratio of 0.07 piezoelectric actuator par cm².

REFERENCES

[1] C. Li *et al.*, « A Modified Neutral Point Balancing Space Vector Modulation for Three-Level Neutral Point Clamped Converters in High-Speed Drives », *IEEE Trans. Ind. Electron.*, vol. 66, nº 2, p. 910-921, févr. 2019, doi: 10.1109/TIE.2018.2835372.

[2] B. Sarlioglu et C. T. Morris, « More Electric Aircraft: Review, Challenges, and Opportunities for Commercial Transport Aircraft », *IEEE Trans. Transp. Electrification*, vol. 1, nº 1, p. 54-64, juin 2015, doi: 10.1109/TTE.2015.2426499.

[3] « Aviation Maintenance Technician Handbook - Airframe Volume 2 », p. 564.

[4] Robert D. Goehner, Norman I. Glover, et Donald G. Hensley, « ELECTRO-IMPULSE DE-CING SYSTEM FOR AIRCRAFT », 4,678,144, 7 juillet 1987

[5] Richard Alexander Olson et Mark Ronald Bridgeford, « ELECTRO-EXPULSIVE DE-CING SYSTEM FOR AIRCRAFT AND OTHER APPLICATIONS », US 2010/0288882 A1, 18 novembre 2010

[6] P. GONIDEC, J. RAMI, H. MAALIOUNE, R. BILLARD, V. RIGOLET, et J.-D. SAUZADE, « Methode for supplying electric power to a nacelle defrosting system and ice protection system through ultrasound », WO 2019/180361 A1, 26 septembre 2019

[7] S. Ramanathan, V. V. Varadan, et V. K. Varadan, « Deicing of helicopter blades using piezoelectric actuators », présenté à SPIE's 7th Annual International Symposium on Smart Structures and Materials, V. K. Varadan, Éd., Newport Beach, CA, juin 2000, p. 281-292. doi: 10.1117/12.388906.

[8] S. V. Venna, Y.-J. Lin, et G. Botura, « Piezoelectric Transducer Actuated Leading Edge De-Icing with Simultaneous Shear and Impulse Forces », *J. Aircr.*, vol. 44, nº 2, p. 509-515, mars 2007, doi: 10.2514/1.23996.

[9] S. Struggl, J. Korak, et C. Feyrer, « A basic approach for wing leading deicing by smart structures », présenté à SPIE Smart Structures and Materials + Nondestructive Evaluation and Health Monitoring, M. Tomizuka, Éd., San Diego, California, USA, mars 2011, p. 79815L. doi: 10.1117/12.880470.

[10] S. B. Kandagal et K. Venkatraman, « Piezo-Actuated Vibratory Deicing of a Flat Plate », in *46th AIAA/ASME/ASCE/AHS/ASC Structures, Structural Dynamics and Materials Conference*, Austin, Texas: American Institute of Aeronautics and Astronautics, avr. 2005. doi: 10.2514/6.2005-2115.

[11] E. Villeneuve, D. Harvey, D. Zimcik, R. Aubert, et J. Perron, « Piezoelectric Deicing System for Rotorcraft », *J. Am. Helicopter Soc.*, vol. 60, nº 4, p. 1-12, oct. 2015, doi: 10.4050/JAHS.60.042001.

[12] M. Budinger, V. Pommier-Budinger, G. Napias, et A. Costa Da Silva, « Ultrasonic Ice Protection Systems: Analytical and Numerical Models for Architecture Tradeoff », *J. Aircr.*, vol. 53, nº 3, p. 680-690, mai 2016, doi: 10.2514/1.C033625.

[13] M. Budinger, V. Pommier-Budinger, A. Reysset, et V. Palanque, « Electromechanical Resonant Ice Protection Systems: Energetic and Power Considerations », *AIAA J.*, vol. 59, nº 7, p. 2590-2602, juill. 2021, doi: 10.2514/1.J060008.

[14] M. Budinger, V. Pommier-Budinger, G. Napias, et A. Costa da Silva, « Ultrasonic Ice Protection Systems: Analytical and Numerical Models for Architecture Tradeoff », *J. Aircr.*, vol. 53, nº 3, p. 680-690, mai 2016, doi: 10.2514/1.C033625.

[15] A. M. A. Mohamed et M. Farzaneh, « An experimental study on the tensile properties of atmospheric ice », *Cold Reg. Sci. Technol.*, vol. 68, nº 3, p. 91-98, sept. 2011, doi: 10.1016/j.coldregions.2011.06.012.

[16] S. R. J. et C. M. L., « Structural properties of impact ices accreted on aircraft structures.pdf ». 1 janvier 1987.

[17] P. H. Gammon, H. Kiefte, M. J. Clouter, et W. W. Denner, « Elastic Constants of Artificial and Natural Ice Samples by Brillouin Spectroscopy », *J. Glaciol.*, vol. 29, nº 103, p. 433-460, 1983, doi: 10.3189/S0022143000030355.

[18] U. Nakaya, « Visco-elastic Properties of Snow and Ice in Greenland Ice Cap ».

[19] J. Druez, C. L. Phan, J. L. Laforte, et D. D. Nguyen, « The Adhesion of Glaze and Rime on Aluminium Electrical Conductors », *Trans. Can. Soc. Mech. Eng.*, vol. 5, nº 4, p. 215-220, déc. 1978, doi: 10.1139/tcsme-1978-0033.

[20] J. J. Petrovic, « Review Mechanical properties of ice and snow ».

[21] « The adhesion and strength properties of ice », *Proc. R. Soc. Lond. Ser. Math. Phys. Sci.*, vol. 245, nº 1241, p. 184-201, juin 1958, doi: 10.1098/rspa.1958.0076.

[22] C. Laforte et J.-L. Laforte, « Deicing Strains and Stresses of Iced Substrates », *J. Adhes. Sci. Technol.*, vol. 26, nº 4-5, p. 603-620, mars 2012, doi: 10.1163/016942411X574790.

[23] F. Guerin, C. Laforte, M.-I. Farinas, et J. Perron, « Analytical model based on experimental data of centrifuge ice adhesion tests with different substrates », *Cold Reg. Sci. Technol.*, vol. 121, p. 93-99, janv. 2016, doi: 10.1016/j.coldregions.2015.10.011.
[24] H. H. G. JeUinek, « ADHESIVE PROPERTIES OF ICE ».
[25] M. Budinger, V. Pommier-Budinger, L. Bennani, P. Rouset, E. Bonaccurso, et F. Dezitter, « Electromechanical Resonant Ice Protection Systems: Analysis of Fracture Propagation Mechanisms », *AIAA J.*, vol. 56, nº 11, p. 4412-4422, nov. 2018, doi: 10.2514/1.J056663.
[26] E. Villeneuve, C. Volat, et S. Ghinet, « Numerical and Experimental Investigation of the Design of a Piezoelectric De-Icing System for Small Rotorcraft Part 1/3: Development of a Flat Plate Numerical Model with Experimental Validation », *Aerospace*, vol. 7, nº 5, p. 62, mai 2020, doi: 10.3390/aerospace7050062.
[27] J. L. Palacios et E. C. Smith, « Investigation of an Ultrasonic Ice Protection System for Helicopter Rotor Blades ».
[28] J. Palacios, E. Smith, J. Rose, et R. Royer, « Ultrasonic De-Icing of Wind-Tunnel Impact Icing », *J. Aircr.*, vol. 48, nº 3, p. 1020-1027, mai 2011, doi: 10.2514/1.C031201.
[29] M. Jomaa, D. Vasic, F. Costa, P.-E. Levy, et M. Ali, « Driving power supply for an avionic piezoelectric deicing system », in *Active and Passive Smart Structures and Integrated Systems XVII*, S. Tol, M. A. Nouh, S. Shahab, J. Yang, et G. Huang, Éd., Long Beach, United States: SPIE, avr. 2023, p. 90. doi: 10.1117/12.2657036.
[30] Rongyuan Li, N. Frohleke, et J. Bocker, « LLCC-PWM inverter for driving high-power piezoelectric actuators », in *2008 13th International Power Electronics and Motion Control Conference*, Poznan, Poland: IEEE, sept. 2008, p. 159-164. doi: 10.1109/EPEPEMC.2008.4635261.
[31] K. Agbossou, J.-L. Dion, S. Carignan, M. Abdelkrim, et A. Cheriti, « Class D amplifier for a power piezoelectric load », *IEEE Trans. Ultrason. Ferroelectr. Freq. Control*, vol. 47, nº 4, p. 1036-1041, juill. 2000, doi: 10.1109/58.852087.
[32] H. L. Cheng, C. A. Cheng, C. C. Fang, et H. C. Yen, « Single-switch high power factor inverter for driving piezoelectric ceramic transducer », in *2009 International Conference on Power Electronics and Drive Systems (PEDS)*, Taipei: IEEE, nov. 2009, p. 1571-1576. doi: 10.1109/PEDS.2009.5385732.
[33] Sai Chun Tang et G. T. Clement, « A harmonic cancellation technique for an ultrasound transducer excited by a switched-mode power converter », in *2008 IEEE Ultrasonics Symposium*, Beijing, China: IEEE, nov. 2008, p. 2076-2079. doi: 10.1109/ULTSYM.2008.0513.
[34] C. Kauczor et N. Frohleke, « Inverter topologies for ultrasonic piezoelectric transducers with high mechanical Q-factor », in *2004 IEEE 35th Annual Power Electronics Specialists Conference (IEEE Cat. No.04CH37551)*, Aachen, Germany: IEEE, 2004, p. 2736-2741. doi: 10.1109/PESC.2004.1355265.
[35] M. Jomaa, F. Costa, D. Vasic, P.-E. Lévy, et M. Ali, « Driving Power Supply for Ultrasound Piezoelectric Transducers », in *2023 IEEE International Conference on Electrical Systems for Aircraft, Railway, Ship Propulsion and Road Vehicles & International Transportation Electrification Conference (ESARS-ITEC)*, Venice, Italy: IEEE, mars 2023, p. 1-5. doi: 10.1109/ESARS-ITEC57127.2023.10114888.
[36] D. M. Divan, « The resonant DC link converter-a new concept in static power conversion », *IEEE Trans. Ind. Appl.*, vol. 25, nº 2, p. 317-325, avr. 1989, doi: 10.1109/28.25548.
[37] D. C. Katsis, J.-Y. Choi, D. Boroyevich, et F. C. Lee, « Drive Cycle Evaluation of A Soft-Switched Electric Vehicle Inverter », p. 6.
[38] J.-Y. Lim, J. Soh, et R.-Y. Kim, « An Improved Single-Phase Zero-Voltage Transition Soft-Switching Inverter with a Subtractive Coupled Inductor Auxiliary Circuit », in *2016 IEEE Vehicle Power and Propulsion Conference (VPPC)*, Hangzhou, China: IEEE, oct. 2016, p. 1-6. doi: 10.1109/VPPC.2016.7791610.
[39] R. W. De Doncker et J. P. Lyons, « The auxiliary resonant commutated pole converter », in *Conference Record of the 1990 IEEE Industry Applications Society Annual Meeting*, Seattle, WA, USA: IEEE, 1990, p. 1228-1235. doi: 10.1109/IAS.1990.152341.
[40] R. Teichmann et S. Bernet, « Investigation and comparison of auxiliary resonant commutated pole converter topologies », in *PESC 98 Record. 29th Annual IEEE Power Electronics Specialists Conference (Cat. No.98CH36196)*, Fukuoka, Japan: IEEE, 1998, p. 15-23. doi: 10.1109/PESC.1998.701873.
[41] W. McMurray, « Resonant snubbers with auxiliary switches », *IEEE Trans. Ind. Appl.*, vol. 29, nº 2, p. 355-362, avr. 1993, doi: 10.1109/28.216544.
[42] S. Delbeea, J. Fontane, N. Gourdain, H. Mugnier, T. Planès, et F. Simatos, « AVIATION AND CLIMATE, a literature reviiew ». mai 2022.
[43] O. Meier et D. Scholz, « Estimation of Power Requirements for Electrical De-Icing Systems », p. 9.

Modar JOMAA received his Engineering degree and Master's degree in Power Electronics from the ENSEEIHT engineering school and Paul Sabatier University, Toulouse, France, in 2020. He is currently working towards the Ph.D. degree with the French aeronautical group Safran, and SATIE laboratory, ENS Paris-Saclay, France. His research interests include power electronics for soft-switching inverters and related EMC in aeronautical applications.

Pierre-Etienne LÉVY received his Master's degree and his Ph. D from the Ecole Normale Supérieure de Cachan in France. He is currently working as an Assistant Professor in electrical engineering at ENS Paris-Saclay in France. His main research topics include power electronics converters and electromagnetic compatibility.

Dejan Vasic obtained his agregation, master's, and doctoral degrees, all in electrical engineering, from the Ecole Normale Superieure de Cachan, France, in 1998, 2000, and 2003, respectively. He is currently a Full Professor of electrical engineering at CY Cergy Paris University, France, and his main research interests lie in the fields of piezoelectric materials for power electronics, dc–dc converters, energy harvesting, and structural damping.

François COSTA (Member, IEEE) received the Ph.D. in electrical engineering from the University Paris-Saclay, France, in 1992. He is a Full Professor in University Paris Est Créteil, France since 2003. He has been the responsible for the master degree in education in sciences & technology in the "Institut National Supérieur du Professorat et de l'Education (INSPE)" between years 2013 to 2019. From 2013 to 2019, he was also heading the "components & systems for electrical energy" department (CSEE) of lab SATIE (35 peoples, ~40 Ph.D. students). Since 2020, he is the director of the laboratory SATIE in university Paris-Saclay

His research fields include high-frequency medium-power converters, EMI issues and modelling, HF instrumentation,

integration of power electronics, piezoelectric converters and low-level energy harvesting systems.

His main activities are focused on EMI in power converters and systems: multi-scales modelling of conducted and radiated emissions (from the component to the system), EMI filter design, EMI modelling of actuators, EMI measurement and characterization of wide bandgap semiconductors.

Marwan Ali was born in Lebanon, in 1985. He received the Master's degree in electromagnetic compatibility for industrial systems from the University Blaise Pascal, Clermont-Ferrand, France, in 2008, and the Ph.D. degree in electrical engineering from Ecole Normale Supérieure de Cachan (ENS), Cachan, France, in 2012. Until 2017, he was doing power electronics research for aircraft applications at SATIE laboratory, AMPERE laboratory and SAFRAN Group. Then, he was a lecturer for a year at CNAM Lebanon. Since 2019, he has been an expert in power electronics and EMC within the Safran Group Research Center (Safran Tech). His research interests include transportation electrification solutions, power electronics, and their integration, design of integrated passives, EMI/EMC, active and passive filters performance, and optimization of EMI hybrid filters.